
Short-term orbital effects of radiation pressure on the Lunar Reconnaissance Orbiter

Dominik Stiller

B.Sc. Student, Faculty of Aerospace Engineering, TU Delft, Netherlands

Abstract

Centimeter-scale orbit determination is necessary for satellite navigation and spaceborne geodesy. Orbits are sensitive to perturbations such as radiation pressure (RP) due to solar radiation as well as planetary albedo and thermal emissions. This project investigated sensitivities of orbit predictions to varying complexity in RP models for the Lunar Reconnaissance Orbiter (LRO). We found that solar RP dominates but lunar RP affects secular variations in semi-major axis and argument of periapsis. A constant-albedo lunar model and a paneled LRO model are recommended for precise radial and along-track positioning.

Acronyms: BRDF bidirectional reflectance distribution function; DLAM-1 Delft Lunar Albedo Model 1; LRO Lunar Reconnaissance Orbiter; RMSE root mean square error; RP radiation pressure; rRMSE relative root mean square error; TUDAT TU Delft Astrodynamics Toolbox

1 Introduction

Describe LRO mission Describe need for POD

sub-meter accuracy in radial component [1] 50-100 m in total position [2]

figure with magnitudes of perturbations

"SRP is the largest non-gravitational perturbation affecting the LRO orbit and inadequate modeling of SRP is the primary cause of large prediction errors for LRO, particularly during high-beta angle periods" [3] albedo modeling on moon necessary for selenodetic mapping [4] albedo radiation significant on moon since no atmosphere exists and surface of lunar highlands is rather reflective % [4] High OD error during full-sun periods with cannonball model, but acceptable with multi-panel model and real attitude for SA and HGA [5]

present similar papers like VielbergKusche

in this paper, only investigate orbital variations over 2.5 day arc - ζ goal is to improve force models for POD Long-term effect of RP would also be interesting (forces could cancel out over time or always act in same direction), but not considered here

TU Delft Astrodynamics Toolbox (Tudat) is used and models are used for future research

when adding acceleration magnitudes, add ref in simulation setup

2 Radiation pressure modeling

RP modeling needs to consider the causes and effects of radiation. This section presents a range of cooperating models for both that can be flexibly composed.

2.1 Mechanics of radiation pressure

RP results from the momentum transfer between electromagnetic radiation and a surface. A spacecraft may receive such radiation from the Sun but also from other celestial bodies: planets and moons emit albedo radiation through reflection of sunlight and thermal radiation depending on surface temperature. The RP exerts a force on the spacecraft governed by surface properties such as area, reflectivity and absorptivity. The resulting acceleration is the result of a complex interplay of the bodies emitting radiation (the "sources") and the spacecraft receiving the radiation (the "target").

Radiation can be characterized by the radiant flux density, which commonly has units of W/m^2 . Radiosity is the *emitted and reflected* radiant flux density of an opaque surface. The irradiance E is the *incident* radiant flux density on a surface and provides a convenient way to decouple source and target models: the irradiance and the direction of incidence are sufficient to determine the target acceleration, independent of the actual source. We can combine this information into a vector quantity which we call directional irradiance $\mathbf{E} = E\hat{\mathbf{r}}_{t/s}$, where $\hat{\mathbf{r}}_{t/s}$ is the unit vector in the source-to-target direction. One or more directional irradiances, which can be thought of as light rays, are the output of a source model and used as input to the target model. The RP exerted on an irradiated surface is proportional to $1/c$, where $c = 299\,792\,458 \text{ m/s}$ is the speed of light. Given the magnitude of c , RP is usually small (around $4.5 \times 10^{-6} \text{ N/m}^2$ for solar radiation at Earth, where $E = 1361 \text{ W/m}^2$ [6]).

Electromagnetic radiation is often composed not just of a single wavelength but rather a range of wavelengths. The distribution can be described by the spectral irradiance in units of $\text{W}/(\text{m}^2 \text{ Hz})$. Since surface properties are often wavelength-dependent, the target model would also have to be aware of the distribution. However, the surface properties as a function of wavelength are often not known, which is also the case for LRO. Therefore, we assume the irradiance

⁰Email: dstiller@uw.edu

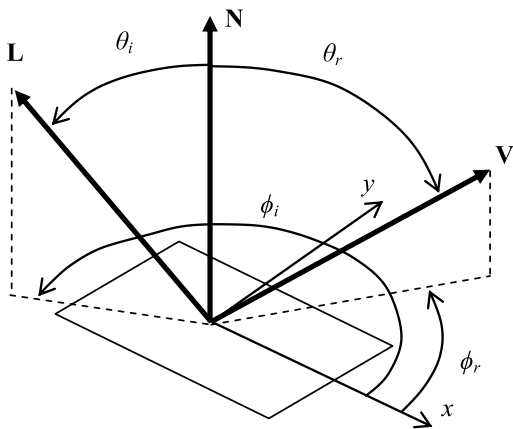


Figure 1. Geometry of a BRDF for a surface with normal \mathbf{N} , incoming direction \mathbf{L} , and observer direction \mathbf{V} . The viewing angle θ_r is between \mathbf{N} and \mathbf{V} . The phase angle (not labeled) is between \mathbf{L} and \mathbf{V} . Adapted from [7].

from source models to be integrated over the whole spectrum and the surface properties of the target model to be valid for all wavelengths.

2.2 Reflectance distribution

Describing the reflectance of a surface is key to RP modeling. Both the way a source reflects sunlight and the direction a target is accelerated in depend on the angular distribution of reflectance.

General reflectance distribution In general, reflectance comprises a diffuse (scattered in many directions) and a specular (mirror-like) component. The remaining energy is absorbed by the surface. The reflectance varies with surface normal \mathbf{N} , incoming radiation direction \mathbf{L} , and observer direction \mathbf{V} . This geometry is shown in Figure 1. A bidirectional reflectance distribution function (BRDF) describes the fraction of irradiance reflected towards the observer per steradian, i.e. [7]

$$f_r(\theta_i, \phi_i, \theta_r, \phi_r) = \frac{dL_r(\theta_r, \phi_r)}{dE_j(\theta_i, \phi_i)}, \quad (1)$$

where dL_r is the reflected radiance (the directional counterpart to radiosity, typically in $\text{W}/(\text{m}^2 \text{sr})$) and dE_j is the received irradiance.

The planetary surface BRDF directly leads to the albedo irradiance received by a target if the sun irradiance at the planet surface and the solid angle subtended by the target are known.

The target surface BRDF gives the direction in which the target is accelerated through integration over all directions \mathbf{V} in which radiation is reflected. The unitless reaction vector, which includes both the direction and magnitude based on absorbed, specularly and diffusely reflected fractions, is therefore [7]

$$\mathbf{R} = - \left[\mathbf{L} + \int_0^{2\pi} \int_0^{\pi/2} f_r \cos \theta_r \mathbf{V} d\theta_r d\phi_r \right]. \quad (2)$$

This vector encapsulates the mechanics of momentum transfer. The reaction is minimal for pure absorption ($f_r = 0$). The reaction is maximal (double the minimum) for pure specular reflection in the incidence direction.

Specular-diffuse reflectance distribution A simplified BRDF is usually more practical for RP modeling: the reflectance is assumed to be a mix of an ideal Lambertian diffuse component and a purely mirror-like specular components. Such a BRDF is given by [7]

$$f_r = C_d \frac{1}{\pi} + C_s \frac{\delta(\mathbf{V} - \mathbf{M})}{\cos \theta_i} \quad (3)$$

where C_d and C_s are the diffuse and specular reflectivity coefficients. Together with the absorption coefficient C_a , energy is conserved when $C_a + C_d + C_s = 1$. The vector $\mathbf{M} = 2 \cos \theta_i \mathbf{N} - \mathbf{L}$ is the direction of \mathbf{L} 's mirror-like reflection, which only contributes if $\mathbf{V} = \mathbf{M}$.

For this simplified BRDF, the integral in Equation (2) evaluates analytically to [8]

$$\mathbf{R} = - \left[(C_a + C_d) \mathbf{L} + \frac{2}{3} C_d \mathbf{N} + 2 \cos \theta_i C_s \mathbf{N} \right]. \quad (4)$$

If the target is in thermodynamic equilibrium, all absorbed radiation is reradiated instantaneously by Kirchhoff's law. If this reradiation is Lambertian, the reaction vector becomes [8]

$$\mathbf{R} = - \left[(C_a + C_d) \left(\mathbf{L} + \frac{2}{3} \mathbf{N} \right) + 2 \cos \theta_i C_s \mathbf{N} \right]. \quad (5)$$

The specular contribution is strictly along the surface normal direction since its tangential components cancel. The Lambertian diffuse contribution (both reflected and reradiated) has a component along the incoming direction but also, weighted by a factor $2/3$ (see [9] for a derivation of this factor), a component along the surface normal. The reaction vector is thus always in the plane spanned by \mathbf{L} and \mathbf{N} .

2.3 Radiation sources

Radiation sources emit or reflect radiation, which exerts RP onto the target. As explained in Section 2.1, the incident radiation at a target due to a source can be thought of as light rays, which are described by their directional irradiance at the target. How the directional irradiance is calculated depends on the type of source.

Isotropic point sources The simplest source model is a point source that isotropically radiates in all directions. This model is appropriate for far-away sources such as the Sun at 1 au distance. Due to the distance, all rays are effectively parallel and can be merged into a single ray parallel to the source-to-target vector $\mathbf{r}_{t/s}$. For an isotropic source, the total luminosity L (units of W) is uniformly distributed over a sphere, leading to an inverse square law. Therefore, the irradiance at the target is

$$E = \frac{L}{4\pi \|\mathbf{r}_{t/s}\|^2}. \quad (6)$$

Alternatively, a reference irradiance E_{ref} observed at a distance \mathbf{r}_{ref} can be scaled:

$$E = E_{\text{ref}} \frac{r_{\text{ref}}}{\|\mathbf{r}_{t/s}\|^2}. \quad (7)$$

The solar luminosity is $3.828 \times 10^{26} \text{ W}$ [10], which corresponds to an irradiance of 1361 W/m^2 at 1 au. Note that these values are averages, which vary with the 11-year solar cycle by about 0.1% and more on shorter timescales due to sunspot darkening and facular brightening [11]. Observational time series exist to account for these variations [12].

Paneled sources: Discretization Radiation due to planets and moons requires more involved source models. Planetary emissions comprise reflected solar radiation and thermal infrared radiation [13]. The fraction of reflected sunlight is called albedo¹ a ; the corresponding type is therefore also called albedo radiation. Thermal radiation is due to absorbed solar energy that is re-emitted in a delayed fashion. Observation time series of albedo and thermal fluxes exist for Earth [12], but physical modeling is required for the Moon.

Since planetary radiation is not isotropic and the spacecraft is typically much closer to the body than to the Sun, the source extent has to be considered. In contrast to the previously described point source, we therefore model Earth and Moon as extended sources. These are discretized into sub-sources, from which rays emanate that are, in general, not parallel. The sub-sources can be thought of as panels with an area, orientation, position, and radiosity model. The panel extent is represented by the area but any other panel properties are only evaluated at its center. A panel only radiates from the positive normal side, not from the backside.

Different algorithms exist to divide the planet ellipsoid into panels. Some authors use a longitude–latitude grid (e.g., [15, 16]), particularly with observed fluxes) or generate static, uniformly spaced panels over the whole sphere (e.g., [7]). However, both approaches are inefficient for low-altitude spacecraft, which require a large number of panels, most of which are never visible. Therefore, the de-facto standard is the dynamic² paneling method introduced by Knocke *et al.* [13].

In Knocke’s method, only the visible area of the planet is paneled. This area is a spherical cap, centered at the subsatellite point and divided into concentric rings that are, again, divided into equal-area segments. A central panel is located at the subsatellite point. All panels contribute to the irradiance received by the target. However, the effective area of each panel is projected by its viewing angle θ_r (see Figure 1) and the irradiance is attenuated by an inverse square law. In Knocke’s method, the rings are spaced such that each panel has the same projected, attenuated area. The projected, attenuated area of a panel is defined as [13]

$$\frac{dA \cos \theta_r}{\|\mathbf{r}_{t/s}\|^2}, \quad (8)$$

where dA is the geometric panel area and $\mathbf{r}_{t/s}$ is the source-to-target vector (in this case, the panel-to-target vector). More rings and more panels per ring improve the fidelity of the calculated irradiance, barring the resolution limit of the radiosity model (e.g., the albedo distribution). While arbitrary numbers of panels per ring are possible, Knocke suggests multiples of 6 (i.e., six panels in the first ring, twelve panels in the second ring, ...). The algorithm is elaborated in [17].

Two examples at different spacecraft altitudes and with different ring numbers are shown in Figure 2. At higher

altitudes, a larger area is visible (approaching a hemisphere) and panels are somewhat more uniform in area. At lower altitudes, the panels are more tightly spaced towards the subsatellite point. In both cases, panel areas increase towards the edge of the visible cap. This pattern is result of the equal projected, attenuated areas.

Paneled sources: Radiosity models The emitted and reflected fluxes of a panel are described by a radiosity model. The irradiance at the target position can then be derived from the panel radiosity. Both radiosity and irradiance commonly have units of W/m^2 . Each panel can have one or more radiosity model, usually one for albedo radiation and one for thermal radiation. We present three such models.

The albedo radiosity model accounts for diffuse Lambertian reflection of solar radiation. It implements the specular-diffuse BRDF from Equation (3) with $C_s = 0$ and the albedo value $C_d = a$ at the panel center. The albedo radiosity of a panel is [13]

$$J_{\text{albedo}} = a (\cos \theta_i)_+ E_s, \quad (9)$$

where E_s is the incoming solar irradiance at the panel (e.g., as found from Equation (6)) and the solar incidence angle θ_i is defined in Figure 1. The operator $(\cdot)_+$ restricts the input to positive values or zero otherwise. This ensures that no radiation is reflected from the backside.

The delayed thermal radiosity model assumes that absorbed radiation is emitted independently of incident solar radiation and the radiosity is thus not a function of θ_i . The only spatial variations arise from emissivity differences. The emissivity e of a surface is the ratio of the actual radiosity to the ideal black body radiosity. The delay arises from the planet’s large thermal inertia. The delayed thermal radiosity of a panel is [13]

$$J_{\text{thermal}} = e \frac{E_s}{4}, \quad (10)$$

where e is the emissivity of the panel, evaluated at its center. The factor 1/4 is the ratio of absorbing area (a circle) to emitting area (a sphere). The albedo and delayed thermal model were originally used by Knocke *et al.* for Earth emissions [13].

The angle-based thermal radiosity model is more appropriate than the delayed model if the surface experience significant diurnal cooling and heating. The surface temperature is modeled as a function of the solar incidence angle θ_i and related to the radiosity through the Stefan–Boltzmann law. The surface temperature is interpolated between the minimum and maximum temperatures, T_{\min} and T_{\max} as

$$T = \max \left(T_{\max} (\cos \theta_i)_+^{1/4}, T_{\min} \right). \quad (11)$$

¹Two types of albedo exist: spherical/Bond albedo is the fraction of sunlight reflected in all directions, while geometrical albedo is the fraction of sunlight reflected with respect to an ideal diffuse surface for normal incidence and viewing directions [14]. For our purpose, spherical albedo is appropriate and synonymous with albedo in this paper.

²Dynamic refers to the fact that panels move with the spacecraft, as opposed to static paneling, for which panels are invariant with spacecraft position or time.

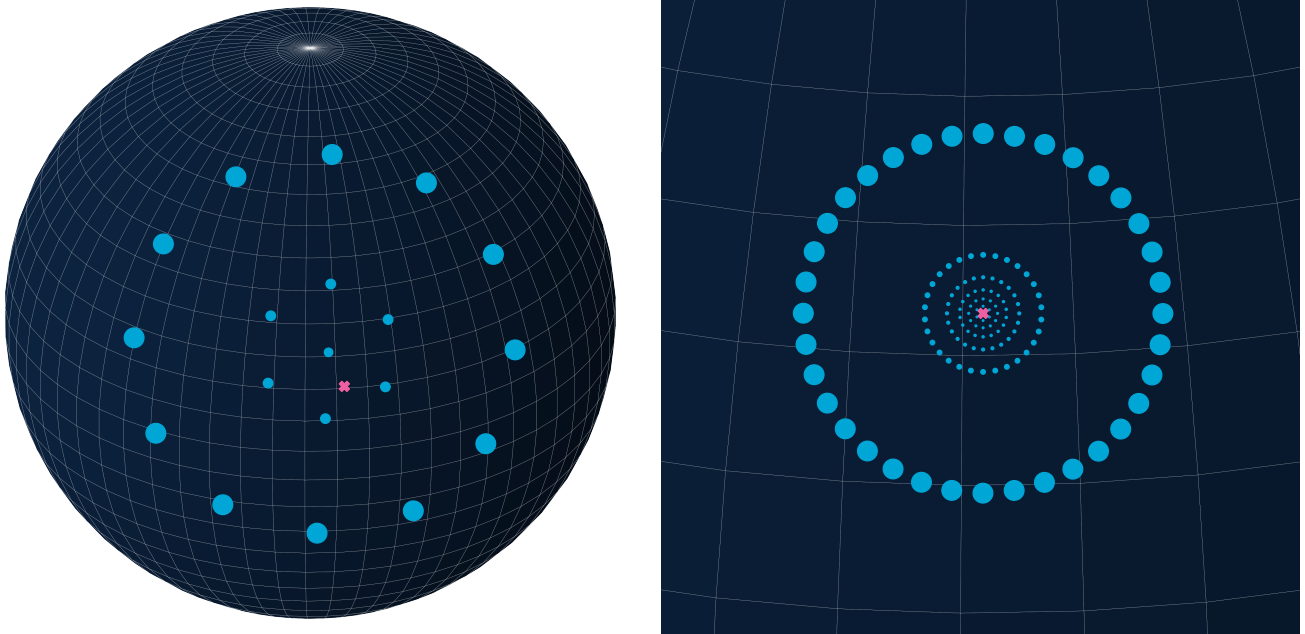


Figure 2. Panels generated with Knocke's algorithm for the Moon, which has a mean radius of 1737 km. The spacecraft (✖) sees a spherical cap (—), which contains rings of panels and is larger at higher altitudes h . Panel centers (●) are scaled proportional to the panel area. The panels have equal projected, attenuated areas and are therefore concentrated around the subsatellite point. The scenario in **b** corresponds to LRO's orbit and the paneling used in this paper.

These temperatures typically correspond to the nighttime temperature and the temperature at the subsolar point. The angle-based thermal radiosity of a panel is then [18]

$$J_{\text{thermal}} = e\sigma T^4, \quad (12)$$

where T is the surface temperature from Equation (11) at the panel center and $\sigma = 5.670 \times 10^{-8} \text{ W}/(\text{m}^2 \text{ K}^4)$ is the Stefan–Boltzmann constant. On the dayside, the radiosity is proportional to $T_{\max}^4 \cos \theta_i$. The maximum radiosity of $e\sigma T_{\max}^4$ is usually larger than the near-constant $eE_s/4$ from Equation (10), but quickly decreases as the panel moves away from the subsolar point (where $\theta_i = 0^\circ$). On the nightside, the thermal radiosity reduces to $e\sigma T_{\min}^4$.

The albedo and thermal radiosity models depend on the distribution of a and e over the planetary surface. The values may be assumed constant but generally vary with longitude, latitude, and time. Particularly for Earth, seasons and weather greatly affect reflectivity and emissivity [19]. Since the Moon lacks seasons, distributions that only vary spatially are appropriate.

To obtain the irradiance at the target due to the panel radiosity, we assume that the emission follows Lambert's cosine law and account for the projected, attenuated area of the source panel. The irradiance therefore is

$$E = \left(\sum_{J_i \in \mathcal{J}} J_i \right) \frac{dA (\cos \theta_r)_+}{\pi \|\mathbf{r}_{t/s}\|^2}, \quad (13)$$

where \mathcal{J} is the set of radiosities from any of the previous radiosity models. Usually, a panel has the albedo model and one thermal model. Here, the source-to-target vector $\mathbf{r}_{t/s}$ uses the panel center position, not the source body center. The direction $\hat{\mathbf{r}}_{t/s}$ of the corresponding directional

irradiance $\mathbf{E} = E\hat{\mathbf{r}}_{t/s}$ is therefore not the same for each panel and thus considers the extent of the source. The radiosities J_i in Equation (13) can be summed since their radiation emanates from the same point, the panel center. Contrarily, the directional irradiances \mathbf{E} can generally not be summed since the their individual directions need to be retained: the reflectance model of the target may be sensitive to the incoming direction of each ray. Therefore, a set of directional radiances \mathcal{E} is handed to the RP target model for acceleration calculations.

2.4 Radiation pressure targets

A RP target is a body that is accelerated by RP. The target model governs how the incident irradiances from point sources and extended sources accelerate the target body.

Cannonball target In its simplest form, a target can be modeled as isotropic sphere, also referred to as cannonball. This sphere is characterized by a cross-sectional area A_c (independent of orientation), radiation pressure coefficient C_r (incorporating reflectivity and absorption coefficients), and mass m . Due to its isotropy, any lateral components cancel and the net acceleration is always along the source-to-target vector. The RP acceleration of a cannonball target is [20]

$$\mathbf{a} = C_r \frac{A_c}{m} \sum_{\mathbf{E}_j \in \mathcal{E}} \frac{\mathbf{E}_j}{c}, \quad (14)$$

where the sum is vectorial and $\sum \mathbf{E}_j/c$ is the total RP as described in Section 2.1. \mathcal{E} is the set of directional irradiances from any number of sources, both point (Equation (6)) and paneled (Equation (13)). The dependence on the area-to-mass ratio A_c/m is similar to drag accelerations. While the cannonball model cannot account for complex geometry,

it is often used in orbit determination with C_r as estimated variable. Ray tracing of a detailed model can also be used to establish the evolution of A_c and C_r [21].

Paneled target In reality, the cross-section and optical properties of a spacecraft change with orientation and incident direction. This effect is particularly noticeable for solar panels, which are large and usually track the Sun. To account for the geometry and differences in materials, a spacecraft can be represented as a collection of n panels. Each panel is characterized by its area, surface normal, and reflectance distribution. The position would only be relevant for rotational but not for linear accelerations. In case of moving parts, the surface normal may change over time. The reflectance distribution can be given as generic BRDF, but is often a specular–diffuse BRDF. The RP acceleration of a paneled target is [22]

$$\mathbf{a} = \frac{1}{m} \sum_{\mathbf{E}_j \in \mathcal{E}} \left(\frac{\|\mathbf{E}_j\|}{c} \sum_{k=1}^n A_k (\cos \theta_{i,k})_+ \mathbf{R}_k \right), \quad (15)$$

where the indices j and k denote the (sub-)source and target panel, respectively. A_k is the area of the k -th panel. $\theta_{i,k}$ is the incidence angle of \mathbf{E}_i onto the k -th panel. \mathbf{R}_k is the reaction vector as defined by Equations (2), (4) or (5), depending on the BRDF. The reaction vector is a function of the panel surface normal \mathbf{N} and the source-to-target direction $\mathbf{L} = \hat{\mathbf{E}}_j$. Therefore, the inner sum has to be evaluated for each directional irradiance \mathbf{E}_j of the outer sum. In general, the resulting acceleration is not along the source-to-target direction as for the cannonball.

Extensions for the paneled target model exist. The model described above does not account for self-shadowing, which occurs when one ray would intersect two panels. This effectively reduces the area of the shadowed panel, an effect that can be significant for complex spacecraft geometries [23]. Polygon intersections enable simple calculation of the effective area [23]. Ray tracing is more involved but can also account for multiple reflections between target panels [24].

Another extension is the radiation pressure due to thermal radiation of the spacecraft itself. Instantaneous reradiation as modeled by Equation (5) for the case of thermodynamic equilibrium is a simple version of this. In reality, panels heat up and cool down (particularly during eclipses) through radiation, conduction, and internal heat production. Advanced models therefore calculate the temperature of each panel. Such models range from a simple heat balance [7] to finite element models [16]. However, lack of knowledge of the thermal properties may restrict the applicability. For the sake of simplicity, neither self-shadowing nor thermal radiation pressure of the spacecraft is considered in this paper.

2.5 Occultation

All previous models assume that the line of sight between source and target is unobstructed. However, occultation is a common astronomical phenomenon: a low-altitude spacecraft may be in the planet's shadow for more than a third of its orbit, and partial or full lunar eclipses can occur multiple times per year. We present two occultation models.

Shadow function The shadow function ν describes the fraction of light received from a spherical source in the

presence of an occulting spherical body. The geometry of the conical occultation model is shown in Figure 3. In the umbra, the source is fully occulted and the observer does not receive any radiation ($\nu = 0$), a state referred to as total eclipse. In the penumbra, the observer can see part of the source ($0 < \nu < 1$). Only outside the shadow region does the observer receive the full radiation ($\nu = 1$). In the case of a lunar eclipse, Earth occults the Sun and casts a shadow onto the Moon such that there is no lunar albedo radiation. On the nightside of a planet, the planet itself occults the Sun.

With the models described in Sections 2.3 and 2.4, the shadow function needs to be considered for radiation from a point source, both when directly incident on the target and when used as solar radiation for albedo radiosity. The extent of the source and occulting bodies needs to be known for shadow function calculations, even in the case of point sources. A derivation of the conical model for ν is presented by Montenbruck and Gill [20].

The conical model can only account for one occulting body. In case of multiple occulting bodies, shadows might overlap and the product of their shadow functions would underestimate the actual received fraction. Knowledge of the shadow intersection would be required to avoid this. Zhang *et al.* derived a model for two occulting bodies [26]. However, only single occultations are considered in this paper.

More involved shadow models exist that improve prediction of the penumbra passage. These models can consider planetary oblateness and atmospheric effects like absorption, scattering and refraction [27]. Other models can account for topography by combining a paneled Sun model with a topography map [28]. These modifications usually prolong the penumbra duration.

Point-to-point visibility For source panels represented by their center point, the shadow function becomes binary: either there is a line of sight between the panel center and the target or there is not. Such point-to-point visibility with a spherical occulting body is easily modeled geometrically. A derivation is given by Vallado and Wertz [25]. Multiple occultations are supported in this occultation model by the logical conjunction of the individual visibilities.

3 Radiation pressure modeling for LRO

TODO write intro

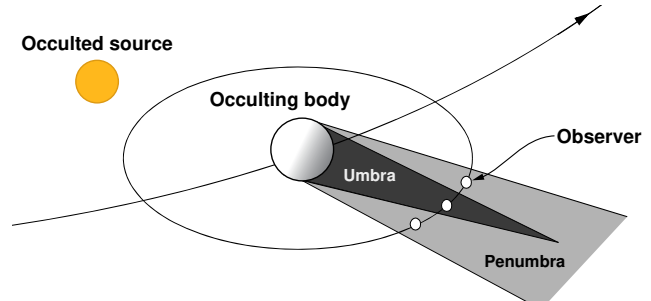


Figure 3. Conical occultation model for spherical sources and occulting bodies. The observer is partially illuminated in the penumbra but fully shadowed in the umbra. Adapted from [25].

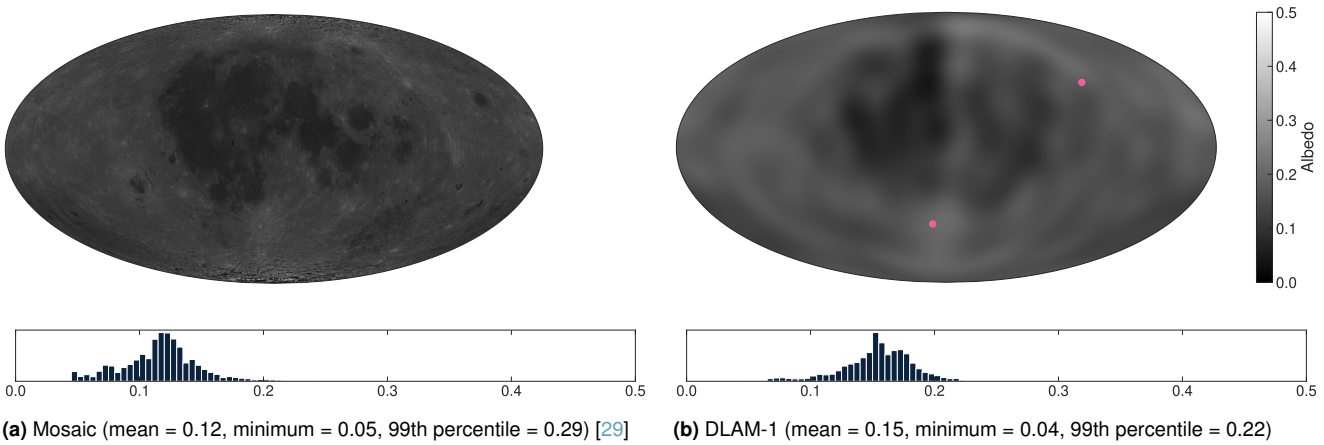


Figure 4. Lunar albedo distribution from Clementine. Both the mosaic and DLAM-1 are based on 750 nm reflectivity, but DLAM-1 has been corrected to the average solar wavelength. Large bright features like the Tycho and Giordano Bruno craters (●) can be registered. Note that the maximum of the albedo scale here is 0.5 instead of 1.0 to increase contrast; in reality, the Moon appears half as bright.

3.1 Lunar albedo radiation

The Moon is a major source of radiation in LRO’s orbit, with lunar irradiance magnitudes approaching half of the Sun’s. Therefore, albedo and thermal radiation due to the Moon is modeled. While the lunar albedo is only 40 % of Earth’s albedo [19], albedo radiation due to the Moon is still substantial, particularly over the subsolar point [4]. Lunar albedo varies significantly with geology: the highlands (mean $a = 0.16$, maximum $a = 0.25$) are much more reflective than the maria (mean $a = 0.07$, minimum $a = 0.05$) due to their respective regolith composition [30–32]. The mosaic of calibrated albedo imagery from Clementine in Figure 4a clearly shows the differences between highlands and marias. The mean of 0.12 agrees with other literature [30], and most of the lunar surface has an albedo below 0.20. Higher values are only found at the poles, where the imagery represents topographic shading rather than actual albedo [33]. Note that the mosaic is for albedo of light at 750 nm wavelength, which is slightly longer than the average solar wavelength. Even though solar radiation has most energy within the 300 nm to 2400 nm band, the spectrum peaks at around 470 nm [34]. Lunar reflectivity increases with increasing wavelength [35].

Floberghagen *et al.*’s 15×15 spherical harmonics expansion called Delft Lunar Albedo Model 1 (DLAM-1) [4] is often used to represent this spatial albedo variability in lunar RP models. DLAM-1 was fitted from Clementine imagery and was designed to work with Knocke’s albedo model for dynamic paneling (Equation (9)). Due to the nature of spherical harmonics, the model cannot resolve features smaller than 12° (360 km at the equator). The expansion is shown in Figure 4b, along with direct imagery from Clementine. DLAM-1 was also derived from 750 nm imagery, but we scale the original values by 1/1.3 to account for the reduced reflectivity at the average solar wavelength. This factor was proposed by Vasavada *et al.* [30]. Even with the correction, the mean albedo of the expansion of 0.15 is still 25 % above the commonly accepted mean of 0.12. This is possibly due to a different calibration of the imagery that DLAM-1 is based on compared to the mosaic from Figure 4a. In fact, Clementine is known to overestimate albedo due to bad calibration [35]. Apart from the difference

in magnitude, the patterns agree reasonably well: maria and highlands are distinct and large bright features like the ray system around the Tycho and Giordano Bruno craters can be recognized (marked in Figure 4b).

Despite the shortcomings of DLAM-1, spherical harmonics are convenient: they are smooth and do not require interpolation like a gridded map. They can easily be truncated to trade detail for computational efficiency. Therefore, we used DLAM-1 in this paper but consider that the magnitude may be overestimated by 25 % during the analysis of results. We also compare results for the location-dependent DLAM-1 with those for a constant value, which should be more computationally efficient. As single representative albedo, we choose the mean of 0.15 instead of 0.12 to facilitate comparison. Note that the spatial variability described above suggests that a single albedo value cannot accurately represent lunar reflectivity.

Albedo radiation assumes ideal, diffuse Lambertian reflectance, which decreases with the cosine of the viewing angle. This assumption is especially appropriate for Earth, for which purely specular radiosity only amounts to 10 % of the purely diffuse radiosity [13]. However, this is not the case for the Moon: the opposition effect increases the reflectance at low phase angles (when the source is behind the observer, see Figure 3) much more than would be expected from a cosine law. In fact, the brightness increases more than 40 % between phase angles of 4° and 0° [36]. This is primarily caused by shadow hiding. To account for non-diffuse reflectance of the lunar surface, the Hapke BRDF was developed [37]. This BRDF is an empirical relation based on nine parameters that control, among other phenomena, the strength and directionality of the opposition effect. Near-global maps for these parameters have been fitted from LRO observations and could be used for a radiosity model [32]. For RP acceleration modeling, the opposition effect is only of concern when the target is above the subsolar point; the Sun has to be in the orbital plane for this. For LRO, this only occurs for a few days twice a year, and even then only for a small fraction of the orbit. Therefore, we neglect the opposition effect in this study.

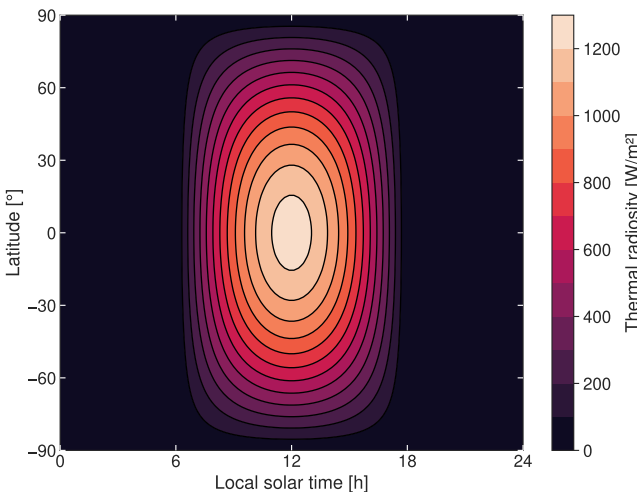


Figure 5. Map of lunar thermal emissions from the angle-based model (Equation (12)). The emissivity is 0.95 and surface temperatures range between 95 K and 385 K, depending on the subsolar angle.

3.2 Lunar thermal radiation

Lunar surface temperatures and the associated thermal radiation undergoes a significant diurnal cycle. Daytime and nighttime temperatures can differ by up to 290 K. The surface heats rapidly after sunrise, cools at about the same rate after local noon, then slower during the night [30]. There are small seasonal changes, with noon temperatures differing by 6 K between lunar aphelion and perihelion [14]. The large diurnal variability makes Knocke's delayed thermal model (Equation (10)), which gives a constant radiosity throughout the day, unsuitable for the Moon.

Diurnal variability is represented well by the angle-based thermal model (Equation (12)). We parametrize the model with the equatorial temperatures just before sunrise ($T_{\min} = 95$ K) and at local noon ($T_{\max} = 385$ K). The model transitions to the nighttime temperature when the incidence angle $\theta_i \geq 89.8^\circ$. The temperatures span a slightly larger range than Lemoine *et al.* ($T_{\min} = 100$ K, $T_{\max} = 375$ K), who initially proposed the angle-based model. However, they agree with those used by Park *et al.* [38]. Note that Park *et al.*'s model is identical up to a factor 1/4 in the radiosity, which is incorrect.

While the albedo varies with location (see Section 3.1), the emissivity and other thermophysical properties are remarkably uniform [31]. This means that a constant emissivity is a fair assumption. We used a value of $e = 0.95$, which is the broadband daytime emissivity, although it decreases to 0.90 during the night [39]. However, we assume the constant daytime emissivity at all times.

The thermal surface radiosity J_{thermal} from the angle-based model with the aforementioned parameters is shown in Figure 5. The radiosity decreases with the cosine of the incidence angle and approaches negligible emissions of 6 W/m² at nighttime. The maximum radiosity, which occurs below the subsolar point (i.e., at local noon), is 1246 W/m². This peak value agrees with those used to design LRO's thermal control subsystem [40]. The only effect that is not captured is the slow cooling by about 25 K between sunset and sunrise [30], which introduces a slight asymmetry;

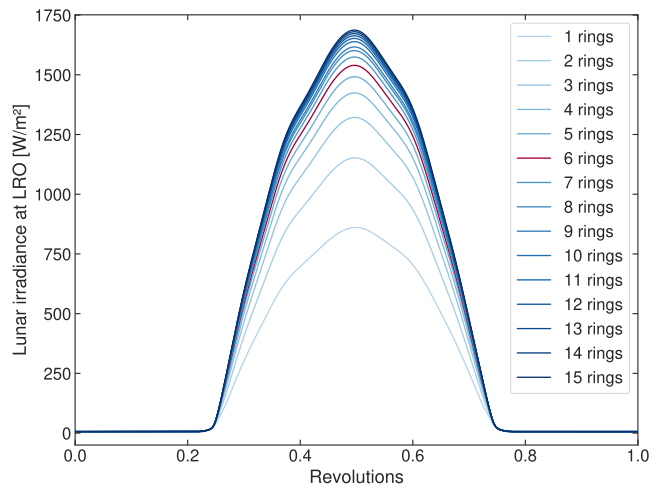


Figure 6. Convergence of lunar irradiance received by LRO for increasing number of rings. Each ring contains six more panels than the previous. Six rings (—) are sufficient for an error of less than 10 % with respect to the converged solution.

constant pre-sunrise temperatures are used throughout the night. We also do not model seasonal variations of surface temperature.

3.3 Paneling of the Moon

The Moon needs to be discretized to evaluate the albedo and thermal radiation numerically. LRO's low altitude compared to the lunar radios prohibits any static paneling, which would have a large number of invisible panels. Therefore, we used Knocke's dynamic paneling method (Section 2.3).

Selecting the number of rings is a trade-off between fidelity and computational efficiency. To determine the lowest number of rings that can still represent lunar radiation with sufficient accuracy, we investigated the convergence behavior. Figure 6 shows the albedo and thermal irradiance E received by LRO for an increasing number of rings. As suggested by Knocke *et al.*, each ring contains six more panels than the previous one. For 13 rings and more, the peak irradiance is within 1 % of 1687 W/m². For six rings, the irradiance peaks at 1540 W/m², which is within 10 % of the converged solution. The results are similar for constant and DLAM-1 albedo.

We choose six rings as sufficiently accurate, which contain 127 panels in total (cf. Figure 2b). This is one ring (or 36 panels) more than used by others. Floberghagen *et al.* suggest five rings for Lunar Prospector, which has twice the orbital altitude of LRO and thus needs fewer rings (Knocke *et al.* used only two rings for a much higher altitude relative to the planetary radius). Five rings are also used for LRO's precision orbit determination [41]. We choose one ring more to keep the error due to paneling below 10 %. More may be required in case of a higher-resolution albedo distribution.

3.4 LRO target

LRO comprises a cubical bus with a large solar array and a protruding high gain antenna (Figure 7). The solar array can be gimbaled partially about the Y and Z axes such that it can track the Sun when it is within LRO's orbit plane; if not, the solar array is at a fixed 45° angle with the -Y bus side.

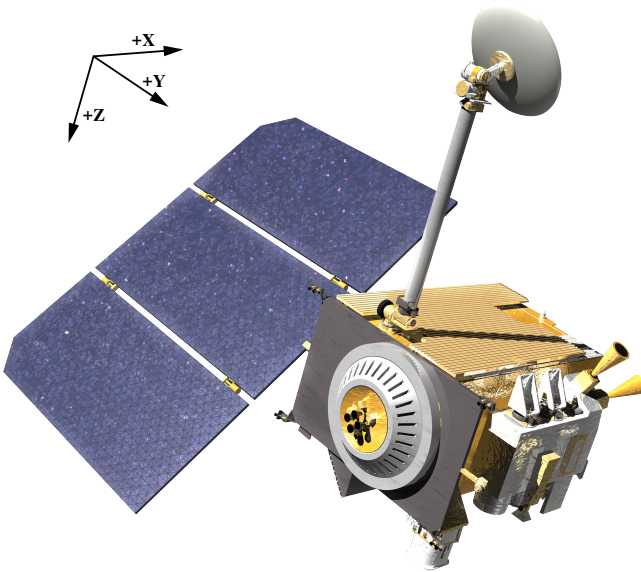


Figure 7. Rendering of LRO [42] with bus frame definition. The X axis is along the velocity vector, the +Y axis is away from the sun, and the +Z axis is in the nadir direction [40].

The antenna points towards Earth whenever it is visible [28]. This leads to large variations in cross-section over time, and different sides are presented to solar and lunar radiation.

LRO can be modeled as paneled target (Equation (15)) to account for this variability. The panels are summarized in Table 1. There are six panels for the bus, with surface normals along the positive and negative axes of the LRO bus frame (cf. Figure 7). The solar array and high gain antenna are modeled separately, again with frontside and backside panels. The solar array is almost as large as all other panels combined. Panels for the solar array and high gain antenna track the Sun and Earth or have a fixed orientation, as described above. Definitive attitudes of actuated panels are also available but were not used.

We also model LRO as a cannonball (Equation (14)), a model which is often used for orbit determination. Finding a single equivalent cross-section area A_c and coefficient C_r that hold at all times is virtually impossible [25]. Different values for LRO exist in literature: Bauer *et al.* used $A_c = 10 \text{ m}^2$ and $C_r = 1.2$ [44], while Nicholson *et al.* used $A_c = 14 \text{ m}^2$

Table 1. Panels for LRO target model from Smith *et al.* [43]. The coefficients are for absorptivity and specular/diffuse reflectivity. The solar array is by far the largest surface, followed by the Z-facing panels.

Panel	C_a	C_s	C_d	$A [\text{m}^2]$	Tracking
+X	0.49	0.29	0.22	2.82	
-X	0.42	0.39	0.19	2.82	
+Y	0.45	0.32	0.23	3.69	
-Y	0.50	0.32	0.18	3.69	
+Z	0.50	0.32	0.18	5.14	
-Z	0.28	0.54	0.18	5.14	
+SA	0.90	0.05	0.05	11.00	+Sun or fixed
-SA	0.50	0.30	0.20	11.00	-Sun or fixed
+HGA	0.54	0.18	0.28	1.00	+Earth
-HGA	0.93	0.02	0.05	1.00	-Earth

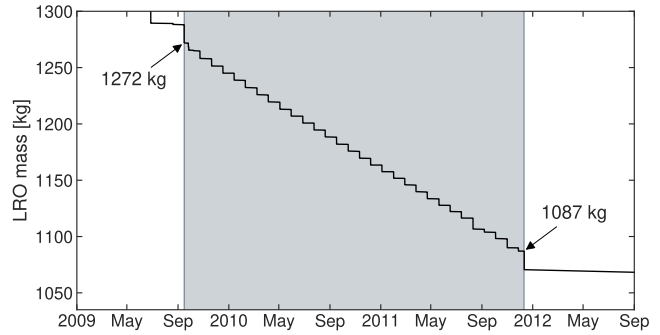


Figure 8. Mass evolution of LRO over the science mission phase (15 September 2009 – 11 December 2011, ■).

and $C_r = 1.0$ [41]. Their acceleration should differ by about 15 %. We choose the latter since it is used for operational orbit estimation of LRO.

To complete the target model, the mass is required to convert forces into accelerations. LRO performed monthly station keeping maneuvers during its science mission phase, which reduced the initial mass after science orbit insertion from 1272 kg to 1087 kg (Figure 8). With every maneuver, 6.3 kg of propellant are expelled [45]. This increases accelerations by 15 % over the course of 21 months. To facilitate comparison and obtain worst-case results, we used the end-of-mission mass of 1087 kg in this paper, independently of the actual arc.

3.5 LRO orbit geometry

LRO's polar science mission orbit has a low altitude of $50 \pm 15 \text{ km}$. The difference between periselene and aposelene is mostly due to a slight eccentricity, but also an equatorial radius that is 2 km larger than the polar radius. The altitude variation affects the lunar irradiance received by LRO. The spacecraft has a period of 113 min.

Visibility of the Sun is determined by the beta angle β , which is the angle between the orbital plane and the Moon-to-Sun vector. It is zero when the Sun is within the plane and $\pm 90^\circ$ when the orbit normal points towards or away from the Sun. Since LRO's orbit is polar, it undergoes all β within a year. For $\beta = 0^\circ$, LRO is moving straight towards and away from the Sun above the poles, experiences the maximum eclipse duration, and passes over the subsolar point. For $\beta = 90^\circ$, LRO is in full view of the Sun throughout the orbit and does not pass over hot or well-illuminated lunar regions. Far large β , LRO's solar array has a fixed orientation as mentioned in Section 3.4. Since the solar array then covers most of the -Y side, self-shadowing of up to 40 % of the total cross-section can occur for solar radiation [28].

Table 2. Orbit geometry for selected arcs over 2.5 days. The June arc has permanent illumination, the September arc the maximum eclipse duration.

	28 June 2010	26 Sept. 2011
Start time (UTC)	15:00:00	18:00:00
$\beta [^\circ]$	88.8 to 88.9	-1.7 to -3.6
Sun distance [au]	1.019	1.000
Eclipse time [min]	0	48
Solar array	Fixed (45° to -Y)	Tracks Sun

Self-shadowing is no issue for small β . In this paper, we neglect self-shadowing, which was shown to only have a minor impact in most cases [3, 46].

Since the effect of RP varies greatly with β , we investigated two contrasting arcs, which are summarized in Table 2. In June, Moon is at aphelion and no eclipses occur since LRO is continuously illuminated at $\beta \approx 90^\circ$. In September, the beta angle is just below 0° so that LRO experiences the maximum solar eclipse duration of 48 min. No lunar eclipses occur during any of the arcs. Both arcs have a length of 2.5 days, which is used for orbit determination of LRO [41, 47]. Choosing the same length ensures our results are relevant for error estimation in force modeling for orbit determination.

3.6 Simulation setup

A range of simulations with varying models is necessary to determine the short-term orbital effects of RP modeling choices. However, a common setup, presented in Table 3, enables comparison. Some things should be clarified:

- Gravity from Jupiter and Venus is neglected since it is 7 orders of magnitude lower than Earth's (TODO add reference to figure).
- Albedo and thermal radiation due to Earth is neglected since it is 3 orders of magnitude lower than the Moon's.
- Occultation of solar radiation through the Moon follows a simple conical model. Time spent in sunlight can be overestimated by up to 480 s for large β if topography is ignored [28].
- No lunar eclipses occur over the two simulation arcs, therefore occultation by Earth can be ignored.
- Good accuracy can be achieved with integration step sizes as high as 15 s [28]. We use 5 s, which is used for operational orbit determination [41].
- While the Moon has a difference between polar and equatorial radius of 2.1 km due to flattening, a perfect sphere will be assumed here to simplify paneling and occultation.
- The Moon Mean Earth/Polar Axis frame is recommended for use with LRO [50].
- LRO SPICE kernels containing ephemerides (SPK) and orientation (CK) are available online³.

4 Results

We analyzed short-term effects of RP on accelerations, position, and Keplerian orbital elements. While position and orbital elements are ultimately relevant for precise orbit determination, examining the accelerations in different scenarios and along the orbit can explain why position and orbital elements changed. Additionally, the accelerations highlight differences between models of varying complexity.

To compare accelerations over one or multiple orbits, we used the root mean square error (RMSE), which is defined as

$$\text{RMSE}(x, y) = \sqrt{\frac{1}{n} \sum_{i=1}^n (x_i - y_i)^2}. \quad (16)$$

The RMSE describes the difference between two scalar timeseries x_i, y_i and gives more weight to large deviations. These scalar timeseries can be the magnitude of accelerations

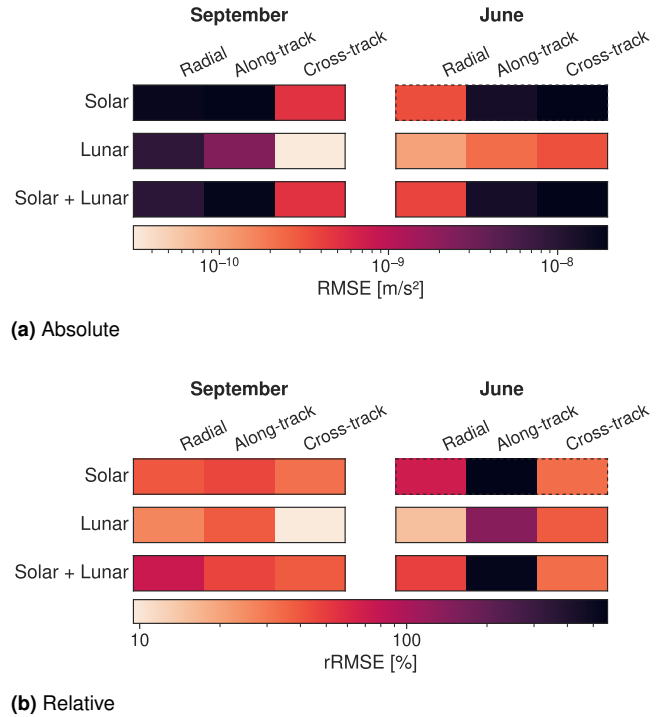


Figure 9. RMS differences of RP accelerations over one orbit with and without instantaneous reradiation. The dashed boxes correspond to Figure 10.

or individual components. The relative root mean square error (rRMSE) is defined as

$$\text{rRMSE}(x, y) = \sqrt{\frac{\sum_{i=1}^n (x_i - y_i)^2}{\sum_{i=1}^n y_i^2}} \quad (17)$$

and is useful to compare differences across orders of magnitude.

While the simulation evaluates accelerations in a global frame, the effect of accelerations on the orbit is best analyzed in a spacecraft-fixed coordinate system that is aligned with the orbital track. The RSW coordinate system is one such system, defined by the unit vectors [25]

$$\mathbf{R} = \frac{\mathbf{r}}{\|\mathbf{r}\|}, \quad \mathbf{W} = \frac{\mathbf{r} \times \mathbf{v}}{\|\mathbf{r} \times \mathbf{v}\|}, \quad \text{and} \quad \mathbf{S} = \mathbf{W} \times \mathbf{R}. \quad (18)$$

The radial component \mathbf{R} is aligned with the planetocentric position vector \mathbf{r} . The cross-track component \mathbf{W} is aligned with the angular momentum vector, or orbit plane normal, involving the linear velocity \mathbf{v} . The along-track component \mathbf{S} completes the right-handed coordinate system. Note that \mathbf{S} is generally not aligned with the velocity vector, only for circular orbits.

4.1 Instantaneous reradiation

First, we investigated the effect of instantaneous reradiation for the paneled target model. This increases the acceleration proportional to each panel's C_a , normal to the panel (cf. Equation (5)).

³https://naif.jpl.nasa.gov/pub/naif/pds/data/lro-l-spice-6-v1.0/lrosp_1000/

Table 3. Common setup for all simulations. Gravity and radiation pressure are the only force models.

Planetary bodies	
Planetary ephemerides	DE 421 [48]
Moon ellipsoid	Sphere of radius 1737.4 km [49] (no flattening)
Moon reference frame	Mean Earth/Polar Axis [50]
Force models	
Moon gravity	GRGM1200L [51] (truncated to 100×100)
Earth + Sun gravity	Central
Solar radiation	Isotropic point source with $L = 3.828 \times 10^{26}$ W [10]
Lunar radiation	Occulted by Moon Paneled source with 6 rings of 6, 12, 18, 24, 30, 36 panels Albedo: Constant $a = 0.150$ or DLAM-1
RP target	Thermal: Angle-based ($e = 0.95$, $T_{\min} = 95$ K, $T_{\max} = 385$ K) Cannonball ($A_c = 14$ m 2 , $C_r = 1.0$) or Paneled (see Table 1) Paneled model with or without instantaneous reradiation Mass: 1087.0 kg (end of science mission) Orientation: LRO_SC_BUS frame from SPICE CK
Simulation settings	
Software	TU Delft Astrodynamics Toolbox (Tudat) 2.12.1.dev19
Propagation frame	ECLIPJ2000
Propagation method	Cowell
Integration method	Runge–Kutta–Fehlberg 7(8)
Step size	5 s (fixed)
Arc length	2.5 days (31.9 revolutions)
Initial state	Cartesian state from SPICE SPK (lrorg_*)

Figure 10 shows the absolute and relative differences between accelerations without and with instantaneous reradiation. In absolute terms, the radial and along-track components are impacted most for the September arc, while the along-track and cross-track components experience the largest increase for the June arc (for both arcs, up to about 1.9×10^{-8} m/s 2 RMSE). The relative differences are more uniform (around 40 % rRMSE), but the along-track components of lunar and solar radiation in the June arc increase by 140 % and 570 % rRMSE, respectively. In most cases, only the magnitude of accelerations changes but not their pattern.

Figure 10 shows the solar radiation of the June arc, the only of our simulations for which the pattern changed significantly. The phase of the radial acceleration is shifted by about 10 % of the orbital period, which is not the case for the other two components or the acceleration due to lunar radiation. This arc also had the largest relative change in along-track acceleration as described above (highlighted in Figure 9). This change is clearly visible as a constant offset of about 13×10^{-9} m/s 2 .

The large changes seen in some cases are mostly due to the +SA panel, which is highly absorptive ($C_a = 0.90$) and large ($A = 11.00$ m 2). For the June arc, the solar array is angled at 45° with equal components in the cross-track and along-track directions. The Sun is on the same side as the solar array in the cross-track direction. Without instantaneous reradiation, no panel has a significant contribution to the along-track acceleration, so it is quite small at around 2×10^{-9} m/s 2 . With instantaneous reradiation, each panel, and especially the solar array, exerts an acceleration parallel to its normal, which leads to the along-track increase witnessed for the June arc.

Since no reradiation due to spacecraft panels is physically unrealistic and the differences in magnitude are significant when instantaneous reradiation is added, we applied instantaneous reradiation for all other simulations. More sophisticated thermal models involving conduction and internal heat production would likely give more accurate results.

4.2 Simulation setups

Solar with/without Lunar with/without Albedo none/constant/dlam Thermal none/angle-based LRO cannonball/paneled with/without instantaneous reradiation Beta angle/arc

46 simulations

no knowledge of true RP accelerations therefore, compare to baseline

cannonball with fixed Cr and paneled cannot directly be compared

Also use [52] as reference for plots and discussion, especially about relation of acc and change in elements

4.3 Accelerations

All accelerations are given in 10 $^{-9}$ m/s 2 .

Solar and lunar radiation Both solar and lunar radiation are significant but their accelerations may amplify or cancel each other. To compare them, we used a constant albedo model in addition to the thermal model. The accelerations over one orbit are shown in Figure 11. Note that secular variations in orbit geometry can change the magnitude of acceleration components even within one 2.5 day arc but are not shown here.

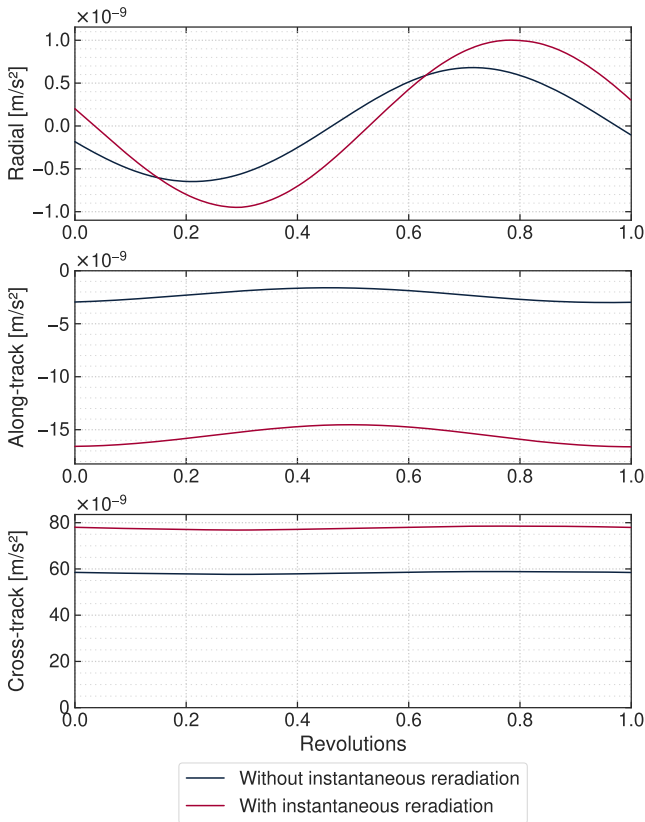


Figure 10. Accelerations due to solar radiation without and with instantaneous reradiation over one orbit for June arc. There is a phase shift in the radial component and the along-track component increased by 570 % RMSE. Lunar contributions and the September arc are not significantly affected in shape.

For the June arc (Figure 11a), the spacecraft is in permanent sunlight and orbit plane normal points towards the sun because $\beta \approx 90^\circ$. This leads to extremely large, constant cross-track solar accelerations. The paneled model also has along-track solar accelerations due to the solar array as explained in Section 4.1. Interestingly, the radial solar accelerations show the same phase shift between the cannonball and paneled target as observed without instantaneous reradiation (Section 4.1). This suggests that symmetry is the cause of the phase shift. The magnitude of the total solar acceleration does not change much throughout the year since it is only dependent on the Moon–Sun distance, which is relatively constant at 1 au (see Table 2).

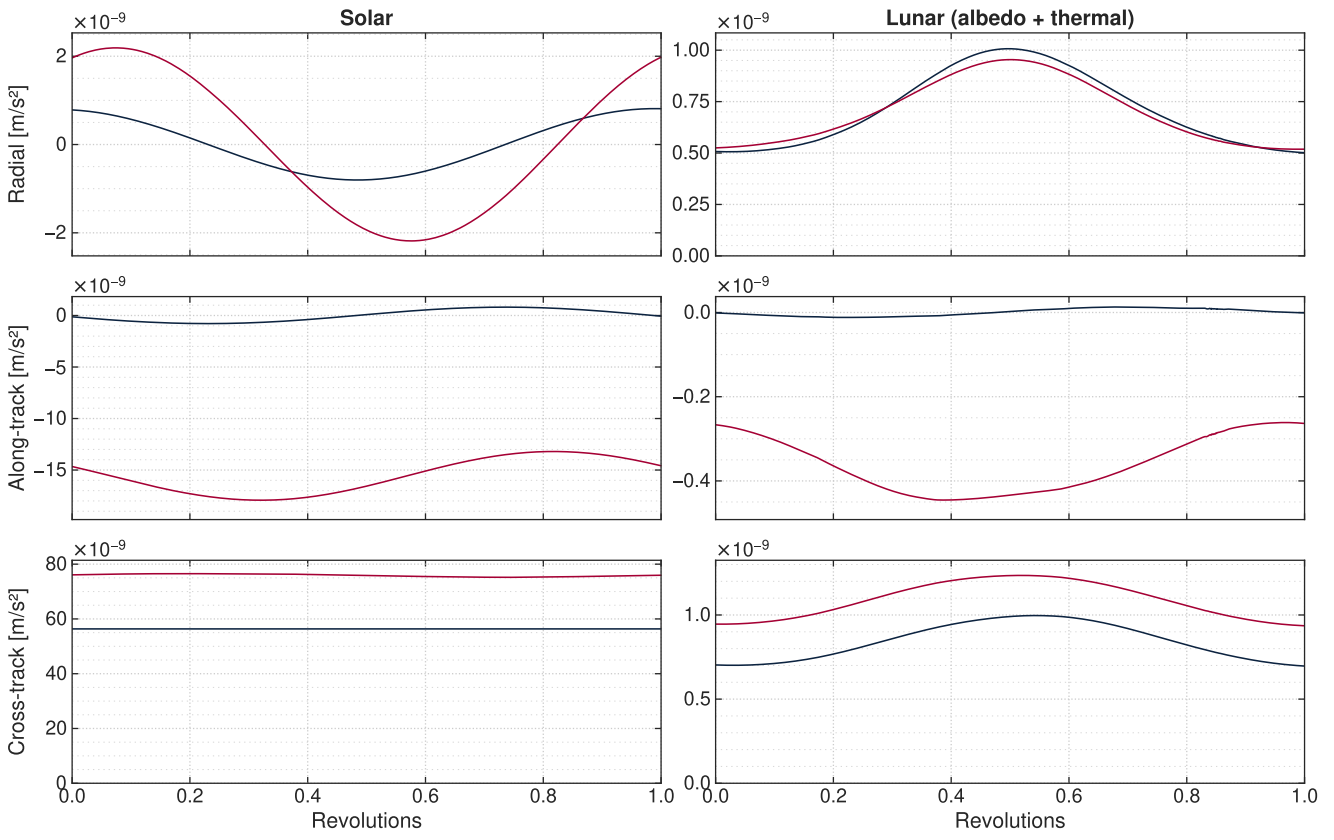
The lunar accelerations during the June arc are generally small (less than 2 % of solar) because LRO never passes over well-illuminated regions; half of the lunar source panels that are visible by LRO are on the nightside and therefore rarely contribute. The variations in lunar radiation pressure are mainly caused by the fact that β is not exactly 90° and LRO's angle to the subsolar point therefore varies by 2° . Secular variations in lunar accelerations (not shown) are due to the evolution of eccentricity over the 2.5 days caused by the non-uniform lunar gravity field [40]. The eccentricity ranges from 0.005 to 0.008, which leads to periselene altitudes between 37 km and 41 km. Changes in eccentricity lead to larger amplitudes but no mean shift. Periodic variations in altitude due to the eccentricity itself have a minimal effect

since higher altitudes mean larger distances but also a larger visible area of the lunar surface, which roughly cancels.

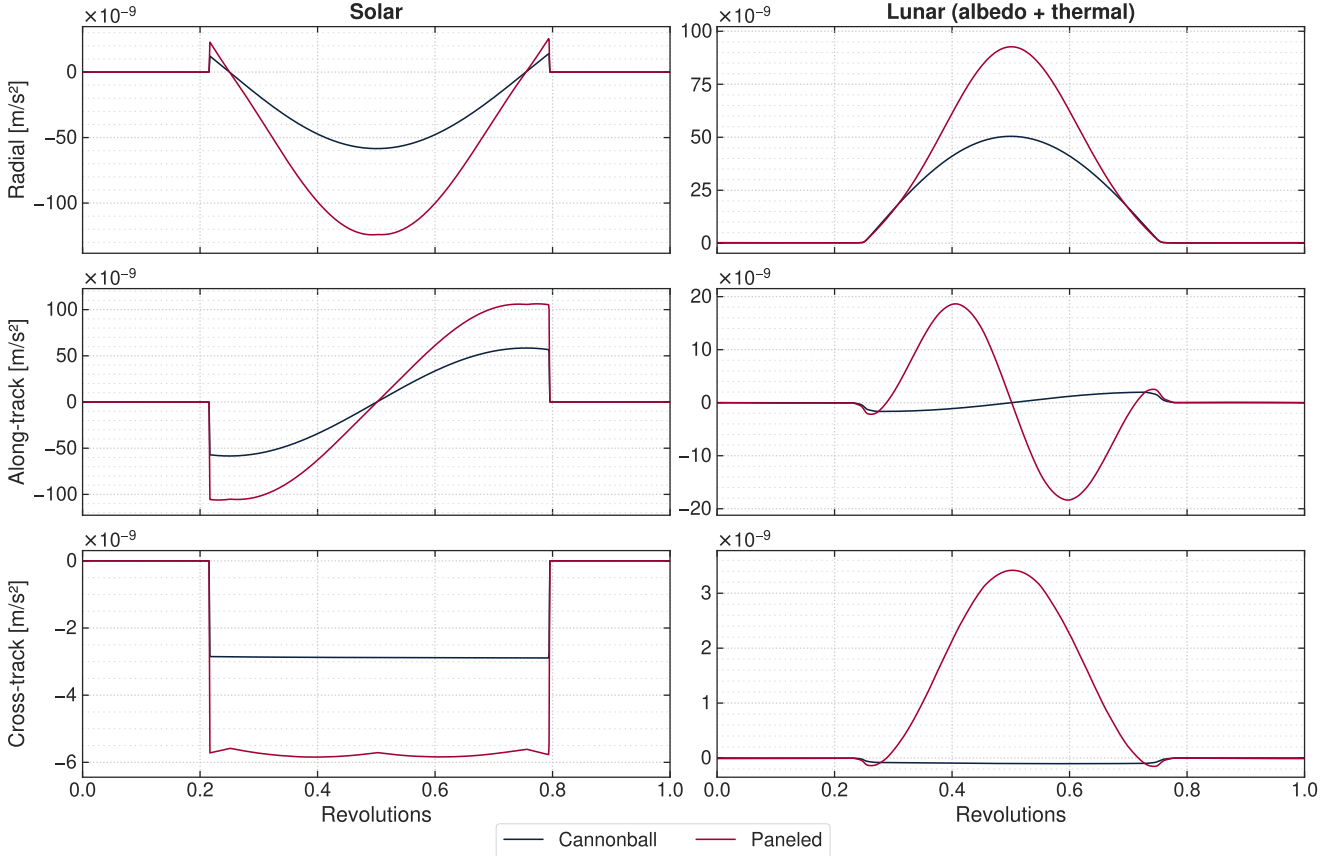
For the September arc (Figure 11b), the Sun is occulted for 42 % of the orbit since $\beta \approx 0^\circ$. The effect of these occultations is clearly visible in solar and lunar radiation, both of which vanish on the nightside. The accelerations are mostly in the radial and along-track directions. This is most clearly explained with the solar accelerations. At 0.2, LRO crosses the terminator above the pole and is moving straight towards the Sun; the along-track component is maximal and negative since the Sun opposes the spacecraft's motion. Continuing the orbit, LRO passes above the subsolar point at 0.5, leading to a maximal and negative radial component while the along-track component has vanished. Further towards the other pole, LRO passes into the night at 0.8, where the along-track component accelerates the spacecraft into the direction of motion. During the whole time, the cross-track component is slightly negative because β is slightly negative but not zero. If β were slightly positive, the cross-track component would be similar but with the sign flipped. The same holds for changes in orbital elements, particularly the inclination and longitude of the ascending node. In addition to periodic changes, there is a secular change in solar accelerations (not shown) since the already slightly negative β continues to decrease: over the 2.5 day arc, the mean of the along-track and cross-track components increase twofold and threefold, respectively. This trend continues until the cross-track component dominates for high β , as seen for the June arc.

The lunar accelerations during the September arc are much larger than during the June arc because LRO passes right over the subsolar point, which reflects much sunlight and has high thermal emissions. Indeed, the lunar irradiance (up to 1831 W/m^2) is larger than the solar irradiance (up to 1362 W/m^2) above the subsolar point. Still, the lunar acceleration magnitude is 14 % smaller than the solar acceleration magnitude since lunar panels are distributed azimuthally around the nadir and thus partially cancel while all solar rays are parallel. Another feature of lunar accelerations is the sign opposite to solar accelerations: when passing over the subsolar point, the radial components of solar and lunar accelerations roughly cancel. A similar effect can be seen in the along-track and cross-track components for a paneled target, although the lunar radiation needs some time to build up. The along-track component peaks at a subsolar angle of 33° , the cross-track component above the subsolar point. The cross-track component increases secularly over the 2.5 day arc, similarly to solar radiation.

Comparing the accelerations of cannonball and paneled targets for both arcs, it is clear that a single C_r cannot capture the complex and changing spacecraft geometry. While the solar accelerations for the September arc are just off by about a constant factor, this is not the case for the June arc or any of the lunar accelerations. In fact, the sign may even be different, particularly for lunar along-track and cross-track accelerations in September. This is likely caused by the solar array tracking the Sun. On smaller scales, the effect of target panels of different size and reflective properties becoming visible as LRO revolves around the Moon can be seen in the shape of the solar cross-track accelerations of the September arc.



(a) June



(b) September

Figure 11. Accelerations due to solar and lunar radiation over one orbit for a paneled target. The cannonball and paneled target differ both in magnitude and pattern of accelerations. Note the different scales of each subplot.

All accelerations are inversely proportional to the spacecraft mass. While we chose the end-of-mission mass for all simulations, the begin-of-mission mass is 17% higher and all accelerations are thus 17% lower (see Section 3.4). This only changes magnitudes, not patterns.

Lunar albedo and thermal radiation due to angle-based model paneled target both affected by occultation

beta angle slightly less than 90 degrees leads to sinusoidal acceleration in June arc

angle-based thermal behaves quite similar to albedo, but does not vanish in eclipse

albedo likely overestimated by 25% as described in Section 3.1

lunar RP dominated by thermal such that variations from DLAM1 are too small to have effect

max difference $5 \times 10^{-9} \text{ m/s}^2$, find location on map via lat/lon - ζ corresponds to large deviation from mean in dlam1 maximum occurs before subsolar point

- Self-shadowing, particularly for SRP, can reduce effective cross section by up to 40% [28], effect mostly for solar [23]
- fit new SH albedo model or just use map
- accurate thermal reradiation (e.g. [55])
- account for non-diffuse reflection of lunar surface, i.e. opposition effect due to shadow hiding and coherent backscatter, which can greatly increase irradiance at small phase angles [36] (this would only be relevant at beta = 0 since low phase angles do not occur for large betas; phase angle is low if target is above subsolar point); a map of Hapke parameters exists [32]

4.4 Change in final position

Thermal in the range of a few meters [47]

Thermal lunar radiation may cause an offset of 1-2 meters over an arclength of 2.5 days [44]

not having moon leads to larger decrease because the sun radial component is not cancelled

prediction september: change in arg peri because solar along-track acts fully above poles without being cancelled by lunar rad

for september: sign of change of inclination and lon asc node depends on sign of beta

4.5 Change in orbital element

compare with Gauss perturbing equations (analytical solution to change of osculating elements based on accelerations), e.g. [53, Sec. 3.2]

Keplerian state wrt ECLIPJ2000, not Moon frame!!

4.6 Performance

no special setup like cpu pinning or disabled hyperthreading for benchmarking only on one setup Performance may vary in other situations [54] still, a good indication also mention minimum

albedo model can increase computational demand by several hundred pct [41]

5 Discussion & Conclusion

magnitude affected by:

- wrong mass
- overestimated albedo
- number of rings
- for cannonball, choice of A and C

recommendations on which models to use

Future work:

- account for moon topography for occlusion [28], could otherwise lead to large misrepresentation of eclipses for $\beta > 70^\circ$

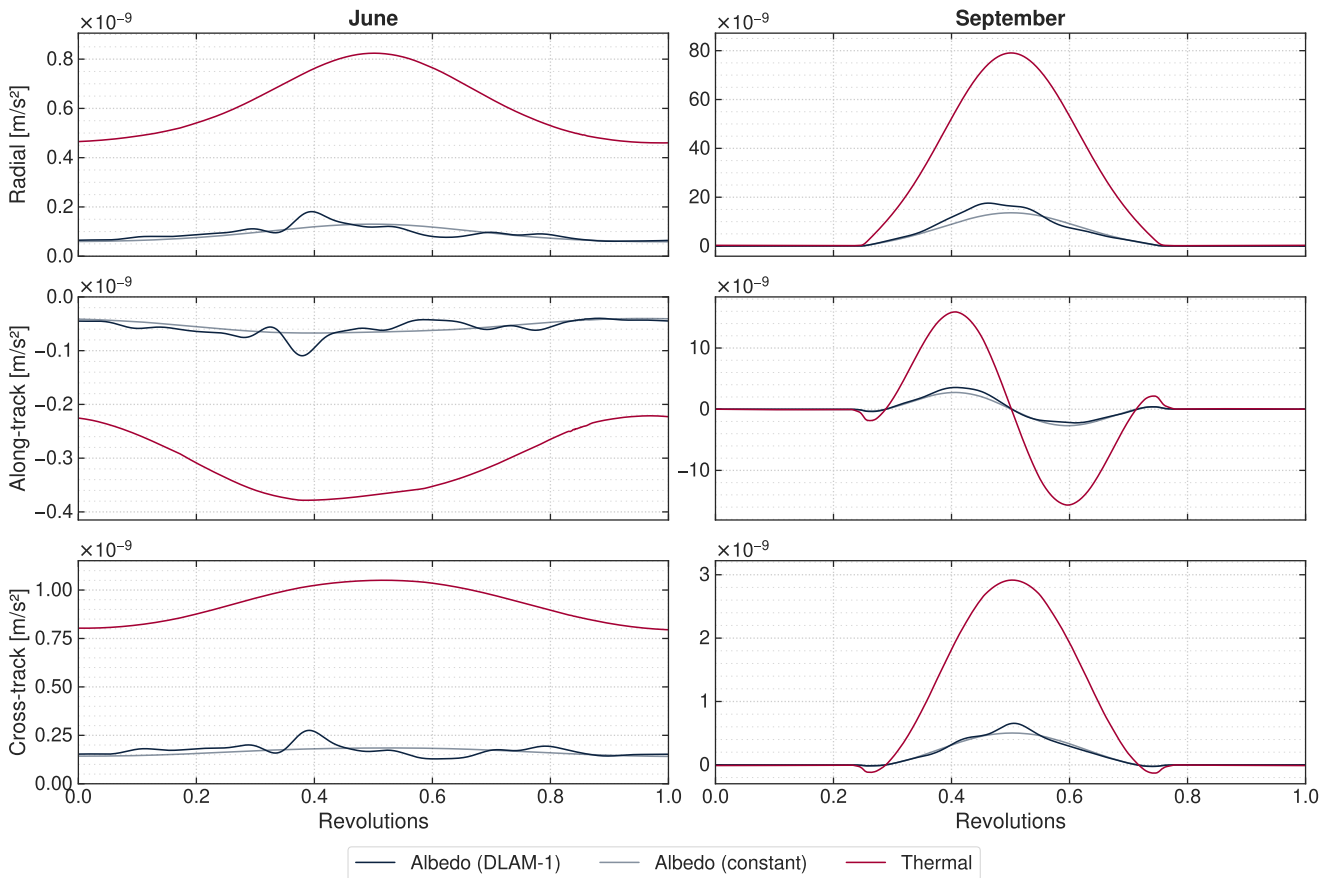


Figure 12. Accelerations due to lunar thermal and albedo radiation. Thermal radiation dominates at all times and the difference between constant and DLAM-1 albedo is small. Note the different scales of each subplot.

References

1. M. T. Zuber *et al.*, “The Lunar Reconnaissance Orbiter Laser Ranging Investigation,” *Space Science Reviews*, vol. 150, no. 1-4, pp. 63–80, May 2009. DOI: [10.1007/s11214-009-9511-z](https://doi.org/10.1007/s11214-009-9511-z).
2. G. Chin *et al.*, “Lunar Reconnaissance Orbiter Overview: The Instrument Suite and Mission,” *Space Science Reviews*, vol. 129, no. 4, pp. 391–419, May 2007. DOI: [10.1007/s11214-007-9153-y](https://doi.org/10.1007/s11214-007-9153-y).
3. S. Slojkowski, J. Lowe, and J. Woodburn, “Orbit determination for the lunar reconnaissance orbiter using an extended Kalman filter,” in *International Symposium on Space Flight Dynamics (ISSFD) 2015*, 2015.
4. R. Floberghagen, P. Visser, and F. Weischede, “Lunar albedo force modeling and its effect on low lunar orbit and gravity field determination,” *Advances in Space Research*, vol. 23, no. 4, pp. 733–738, Jan. 1999. DOI: [10.1016/s0273-1177\(99\)00155-6](https://doi.org/10.1016/s0273-1177(99)00155-6).
5. S. E. Slojkowski, “Lunar Reconnaissance Orbiter orbit determination accuracy analysis,” in *International Symposium on Space Flight Dynamics*, 2014.
6. G. Kopp and J. L. Lean, “A new, lower value of total solar irradiance: Evidence and climate significance,” *Geophysical Research Letters*, vol. 38, no. 1, n/a–n/a, Jan. 2011. DOI: [10.1029/2010gl045777](https://doi.org/10.1029/2010gl045777).
7. C. J. Wetterer *et al.*, “Refining Space Object Radiation Pressure Modeling with Bidirectional Reflectance Distribution Functions,” *Journal of Guidance, Control, and Dynamics*, vol. 37, no. 1, pp. 185–196, Jan. 2014. DOI: [10.2514/1.60577](https://doi.org/10.2514/1.60577).
8. O. Montenbruck, P. Steigenberger, and U. Hugentobler, “Enhanced solar radiation pressure modeling for Galileo satellites,” *Journal of Geodesy*, vol. 89, no. 3, pp. 283–297, Nov. 2014. DOI: [10.1007/s00190-014-0774-0](https://doi.org/10.1007/s00190-014-0774-0).
9. M. Ziebart, “Generalized Analytical Solar Radiation Pressure Modeling Algorithm for Spacecraft of Complex Shape,” *Journal of Spacecraft and Rockets*, vol. 41, no. 5, pp. 840–848, Sep. 2004. DOI: [10.2514/1.13097](https://doi.org/10.2514/1.13097).
10. A. Prša *et al.*, “NOMINAL VALUES FOR SELECTED SOLAR AND PLANETARY QUANTITIES: IAU 2015 RESOLUTION B3,” *The Astronomical Journal*, vol. 152, no. 2, p. 41, Aug. 2016. DOI: [10.3847/0004-6256/152/2/41](https://doi.org/10.3847/0004-6256/152/2/41).
11. G. Kopp, “Magnitudes and timescales of total solar irradiance variability,” *Journal of Space Weather and Space Climate*, vol. 6, A30, 2016. DOI: [10.1051/swsc/2016025](https://doi.org/10.1051/swsc/2016025).
12. S. Dewitte and N. Clerbaux, “Measurement of the Earth Radiation Budget at the Top of the Atmosphere—A Review,” *Remote Sensing*, vol. 9, no. 11, p. 1143, Nov. 2017. DOI: [10.3390/rs9111143](https://doi.org/10.3390/rs9111143).

13. P. Knocke, J. Ries, and B. Tapley, "Earth radiation pressure effects on satellites," in *Astroynamics Conference*, American Institute of Aeronautics and Astronautics, Aug. 1988. DOI: [10.2514/6.1988-4292](https://doi.org/10.2514/6.1988-4292).
14. G. Heiken and B. M. French, *Lunar Sourcebook, A User's Guide to the Moon*. Cambridge University Press, 1991.
15. C. J. Rodriguez-Solano, U. Hugentobler, P. Steigenberger, and S. Lutz, "Impact of Earth radiation pressure on GPS position estimates," *Journal of Geodesy*, vol. 86, no. 5, pp. 309–317, Oct. 2011. DOI: [10.1007/s00190-011-0517-4](https://doi.org/10.1007/s00190-011-0517-4).
16. F. Wöske, T. Kato, B. Rievers, and M. List, "GRACE accelerometer calibration by high precision non-gravitational force modeling," *Advances in Space Research*, vol. 63, no. 3, pp. 1318–1335, Feb. 2019. DOI: [10.1016/j.asr.2018.10.025](https://doi.org/10.1016/j.asr.2018.10.025).
17. P. Knocke, "Earth radiation pressure effects on satellites," Ph.D. dissertation, The University of Texas at Austin, 1989.
18. F. G. Lemoine *et al.*, "High-degree gravity models from GRAIL primary mission data," *Journal of Geophysical Research: Planets*, vol. 118, no. 8, pp. 1676–1698, Aug. 2013. DOI: [10.1002/jgre.20118](https://doi.org/10.1002/jgre.20118).
19. P. R. Goode *et al.*, "Earthshine observations of the Earth's reflectance," *Geophysical Research Letters*, vol. 28, no. 9, pp. 1671–1674, May 2001. DOI: [10.1029/2000gl012580](https://doi.org/10.1029/2000gl012580).
20. O. Montenbruck and E. Gill, *Satellite Orbits*. Springer Berlin Heidelberg, Dec. 2000, 371 pp. DOI: [10.1007/978-3-642-58351-3](https://doi.org/10.1007/978-3-642-58351-3).
21. A. Hattori and T. Otsubo, "Time-varying solar radiation pressure on Ajisai in comparison with LAGEOS satellites," *Advances in Space Research*, vol. 63, no. 1, pp. 63–72, Jan. 2019. DOI: [10.1016/j.asr.2018.08.010](https://doi.org/10.1016/j.asr.2018.08.010).
22. J. Marshall, S. Luthcke, P. Antreasian, and G. Rosborough, "Modeling radiation forces acting on TOPEX/Poseidon for precision orbit determination," Goddard Space Flight Center, Tech. Rep. NASA-TM-104564, 1992.
23. E. Mazarico, M. T. Zuber, F. G. Lemoine, and D. E. Smith, "Effects of Self-Shadowing on Nonconservative Force Modeling for Mars-Orbiting Spacecraft," *Journal of Spacecraft and Rockets*, vol. 46, no. 3, pp. 662–669, May 2009. DOI: [10.2514/1.41679](https://doi.org/10.2514/1.41679).
24. P. W. Kenneally and H. Schaub, "Fast spacecraft solar radiation pressure modeling by ray tracing on graphics processing unit," *Advances in Space Research*, vol. 65, no. 8, pp. 1951–1964, Apr. 2020. DOI: [10.1016/j.asr.2019.12.028](https://doi.org/10.1016/j.asr.2019.12.028).
25. D. A. Vallado and J. Wertz, *Fundamentals of Astrodynamics and Applications*, 4th ed. Microcosm Press, 2013, p. 1106.
26. R. Zhang, R. Tu, P. Zhang, J. Liu, and X. Lu, "Study of satellite shadow function model considering the overlapping parts of Earth shadow and Moon shadow and its application to GPS satellite orbit determination," *Advances in Space Research*, vol. 63, no. 9, pp. 2912–2929, May 2019. DOI: [10.1016/j.asr.2018.02.002](https://doi.org/10.1016/j.asr.2018.02.002).
27. Z. Li, M. Ziebart, S. Bhattacharai, and D. Harrison, "A shadow function model based on perspective projection and atmospheric effect for satellites in eclipse," *Advances in Space Research*, vol. 63, no. 3, pp. 1347–1359, Feb. 2019. DOI: [10.1016/j.asr.2018.10.027](https://doi.org/10.1016/j.asr.2018.10.027).
28. E. Mazarico, G. A. Neumann, M. K. Barker, S. Goossens, D. E. Smith, and M. T. Zuber, "Orbit determination of the Lunar Reconnaissance Orbiter: Status after seven years," *Planetary and Space Science*, vol. 162, pp. 2–19, Nov. 2018. DOI: [10.1016/j.pss.2017.10.004](https://doi.org/10.1016/j.pss.2017.10.004).
29. USGS Astrogeology Science Center. "Moon Clementine UVVIS Global Mosaic 118m v2." (Apr. 9, 2009), [Online]. Available: https://astrogeology.usgs.gov/search/map/Moon/Clementine/UVVIS/Lunar_Clementine_UVVIS_750nm_Global_Mosaic_118m_v2.
30. A. R. Vasavada *et al.*, "Lunar equatorial surface temperatures and regolith properties from the Diviner Lunar Radiometer Experiment," *Journal of Geophysical Research: Planets*, vol. 117, no. E12, n/a–n/a, Apr. 2012. DOI: [10.1029/2011je003987](https://doi.org/10.1029/2011je003987).
31. P. O. Hayne *et al.*, "Global Regolith Thermophysical Properties of the Moon From the Diviner Lunar Radiometer Experiment," *Journal of Geophysical Research: Planets*, vol. 122, no. 12, pp. 2371–2400, Dec. 2017. DOI: [10.1002/2017je005387](https://doi.org/10.1002/2017je005387).
32. H. Sato, M. S. Robinson, B. Hapke, B. W. Denevi, and A. K. Boyd, "Resolved Hapke parameter maps of the Moon," *Journal of Geophysical Research: Planets*, vol. 119, no. 8, pp. 1775–1805, Aug. 2014. DOI: [10.1002/2013je004580](https://doi.org/10.1002/2013je004580).
33. A. McEwen and M. Robinson, "Mapping of the Moon by Clementine," *Advances in Space Research*, vol. 19, no. 10, pp. 1523–1533, Jan. 1997. DOI: [10.1016/s0273-1177\(97\)00365-7](https://doi.org/10.1016/s0273-1177(97)00365-7).
34. M. Iqbal, *Introduction to Solar Radiation*. Academic Press Canada, 1983.
35. Y. Shkuratov, V. Kaydash, V. Korokhin, Y. Velikodsky, N. Opanasenko, and G. Videen, "Optical measurements of the Moon as a tool to study its surface," *Planetary and Space Science*, vol. 59, no. 13, pp. 1326–1371, Oct. 2011. DOI: [10.1016/j.pss.2011.06.011](https://doi.org/10.1016/j.pss.2011.06.011).
36. B. J. Buratti, J. K. Hillier, and M. Wang, "The Lunar Opposition Surge: Observations by Clementine," *Icarus*, vol. 124, no. 2, pp. 490–499, Dec. 1996. DOI: [10.1006/icar.1996.0225](https://doi.org/10.1006/icar.1996.0225).
37. B. Hapke, *Theory of reflectance and emittance spectroscopy*. Cambridge University Press, 2012.
38. R. S. Park *et al.*, "Estimating a High-Resolution Lunar Gravity Field and Time-Varying Core Signature," in *AGU Fall Meeting Abstracts*, vol. 2011, Dec. 2011, P44B-06, P44B-06.
39. J. L. Bandfield, P. O. Hayne, J.-P. Williams, B. T. Greenhagen, and D. A. Paige, "Lunar surface roughness derived from LRO Diviner Radiometer observations," *Icarus*, vol. 248, pp. 357–372, Mar. 2015. DOI: [10.1016/j.icarus.2014.11.009](https://doi.org/10.1016/j.icarus.2014.11.009).

40. C. R. Tooley *et al.*, “Lunar Reconnaissance Orbiter Mission and Spacecraft Design,” *Space Science Reviews*, vol. 150, no. 1-4, pp. 23–62, Jan. 2010. DOI: [10.1007/s11214-009-9624-4](https://doi.org/10.1007/s11214-009-9624-4).
41. A. Nicholson, S. Slojkowski, A. Long, M. Beckman, and R. Lamb, “NASA GSFC Lunar Reconnaissance Orbiter (LRO) Orbit Estimation and Prediction,” in *SpaceOps 2010 Conference*, American Institute of Aeronautics and Astronautics, Apr. 2010. DOI: [10.2514/6.2010-2328](https://doi.org/10.2514/6.2010-2328).
42. NASA Science Mission Directorate. “Spacecraft Icons.” (2018), [Online]. Available: <https://science.nasa.gov/get-involved/toolkits/spacecraft-icons>.
43. D. Smith, M. Zuber, F. Lemoine, M. Torrence, and E. Mazarico, “Orbit determination of LRO at the Moon,” in *7th Int. Laser Ranging Service Workshop*, 2008, pp. 13–17.
44. S. Bauer *et al.*, “Demonstration of orbit determination for the Lunar Reconnaissance Orbiter using one-way laser ranging data,” *Planetary and Space Science*, vol. 129, pp. 32–46, Sep. 2016. DOI: [10.1016/j.pss.2016.06.005](https://doi.org/10.1016/j.pss.2016.06.005).
45. M. Mesarch, M. Beckman, D. Folta, R. Lamb, and K. Richon, “Maneuver Operations Results from the Lunar Reconnaissance Orbiter (LRO) Mission,” in *SpaceOps 2010 Conference*, American Institute of Aeronautics and Astronautics, Apr. 2010. DOI: [10.2514/6.2010-1985](https://doi.org/10.2514/6.2010-1985).
46. A. Löcher and J. Kusche, “Precise orbits of the Lunar Reconnaissance Orbiter from radiometric tracking data,” *Journal of Geodesy*, vol. 92, no. 9, pp. 989–1001, Feb. 2018. DOI: [10.1007/s00190-018-1124-4](https://doi.org/10.1007/s00190-018-1124-4).
47. E. Mazarico *et al.*, “Orbit determination of the Lunar Reconnaissance Orbiter,” 3, vol. 86, Springer Science and Business Media LLC, Sep. 2011, pp. 193–207. DOI: [10.1007/s00190-011-0509-4](https://doi.org/10.1007/s00190-011-0509-4).
48. W. M. Folkner, J. G. Williams, and D. H. Boggs, “The planetary and lunar ephemeris DE 421,” *IPN progress report*, vol. 42, no. 178, p. 1, 2009.
49. B. A. Archinal *et al.*, “Report of the IAU Working Group on Cartographic Coordinates and Rotational Elements: 2009,” *Celestial Mechanics and Dynamical Astronomy*, vol. 109, no. 2, pp. 101–135, Dec. 2010. DOI: [10.1007/s10569-010-9320-4](https://doi.org/10.1007/s10569-010-9320-4).
50. Goddard Space Flight Center, “A Standardized Lunar Coordinate System for the Lunar Reconnaissance Orbiter and Lunar Datasets, LRO Project and LGCWG White Paper,” Tech. Rep., Oct. 1, 2008.
51. S. Goossens, Á. F. Mora, E. Heijkoop, and T. J. Sabaka, “Patched Local Lunar Gravity Solutions Using GRAIL Data,” *Earth and Space Science*, vol. 8, no. 11, Oct. 2021. DOI: [10.1029/2021ea001695](https://doi.org/10.1029/2021ea001695).
52. N. Borderies and P.-y. Longaretti, “A new treatment of the albedo radiation pressure in the case of a uniform albedo and of a spherical satellite,” *CELESTIAL MECHANICS AND DYNAMICAL ASTRONOMY*, vol. 49, no. 1, pp. 69–98, 1990. DOI: [10.1007/bf00048582](https://doi.org/10.1007/bf00048582).
53. D. M. Lucchesi and V. Iafolla, “The Non-Gravitational Perturbations impact on the BepiColombo Radio Science Experiment and the key rôle of the ISA accelerometer: direct solar radiation and albedo effects,” *Celestial Mechanics and Dynamical Astronomy*, vol. 96, no. 2, pp. 99–127, Oct. 2006. DOI: [10.1007/s10569-006-9034-9](https://doi.org/10.1007/s10569-006-9034-9).
54. T. Mytkowicz, A. Diwan, M. Hauswirth, and P. F. Sweeney, “Producing wrong data without doing anything obviously wrong!” *ACM SIGPLAN Notices*, vol. 44, no. 3, pp. 265–276, Feb. 2009. DOI: [10.1145/1508284.1508275](https://doi.org/10.1145/1508284.1508275).
55. J. A. Marshall and S. B. Luthcke, “Modeling radiation forces acting on Topex/Poseidon for precision orbit determination,” *Journal of Spacecraft and Rockets*, vol. 31, no. 1, pp. 99–105, Jan. 1994. DOI: [10.2514/3.26408](https://doi.org/10.2514/3.26408).